Journal of Alloys and Compounds 610 (2014) 462–471

Contents lists available at ScienceDirect

Journal of Alloys and Compounds

journal homepage: www.elsevier.com/locate/jalcom

On the microsegregation of Al–Mg alloys by thermal analysis and numerical modeling

M.H. Avazkonandeh-Gharavol [a], M. Haddad-Sabzevar [a,*], H. Fredriksson [b]

[a] Department of Metallurgy and Materials Engineering, Faculty of Engineering, Ferdowsi University of Mashhad, Azadi Square, P.O. Box 91775-1111, Mashhad, Iran
[b] Materials Science and Engineering Department, Royal Institute of Technology, Brinellvägen 23, 100 44 Stockholm, Sweden

ARTICLE INFO

Article history:
Received 24 February 2014
Received in revised form 30 April 2014
Accepted 5 May 2014
Available online 15 May 2014

Keywords:
Binary Al–Mg alloys
Solidification
Differential thermal analysis
Microsegregation
Diffusion coefficient

ABSTRACT

Knowledge about solid fraction versus temperature during solidification is crucial for the control of solidification processes. In the present paper solidification sequence and path of Al–Mg binary alloys containing 6.7 and 10.2 wt.% Mg was investigated by a series of DTA and quenching experiments and numerical modeling in 0.5 and 5 K min^{-1} cooling rates. Experimental results show that at both cooling rates, Al–6.7 wt.% Mg solidifies with a single phase structure, but Al–10.2 wt.% Mg solidifies with a two phase structure. According to the results of numerical modeling, good agreement between calculated solidification curves and experimental solid fractions, but poor correlation with concentration profiles. The source of discrepancies is discussed according to different theories of microsegregation.

1. Introduction

Aluminum alloys are frequently used in automobile and aerospace industries to reduce the weight of components and structures. Al–Mg alloys are one of the major Al alloys which widely used because of their special features such as low density, high resistance to corrosion, good machinability and attractive appearance when anodized. The magnesium contents of the binary Al–Mg alloys range from 4% to 10%. Al–10 wt.% Mg responds to heat treatment and a desirable combination of high strength, ductility and impact resistance may be achieved after heat treatment [1].

Thermal analysis is an efficient method to study the solidification of metals and alloys [2]. Controlling solidification process is very important and understanding the solidification curves, i.e. the solidification sequences and solid fractions versus temperatures during solidification, are crucial for the control of solidification processes [3]. The liquid fraction can affect alloy castability and formability. In particular, the last 10% fractional evolution during casting significantly affects casting defects such as hot tearing and porosity [4]. The direct measurement of the fractional change as a function of temperature is difficult. The amount of liquid is usually estimated either by quantitative image analysis of quenched samples [3,5] or by using enthalpy measurements [4,6].

Casting processes are the most important methods in the manufacturing of aluminum alloys [3]. The solidification behavior of the ingot has a great influence on the mechanical and physical properties of Al alloys. Microsegregation, which is non-uniform distribution of alloying elements in the scale of secondary dendrite arm spacing (SDAS), is one of the most important phenomena occurring during solidification. It usually results in formation of some unexpected second phases which generally reduce the workability of casting products. Because of industrial importance of microsegregation, it has been extensively studied during the last decades both theoretically and experimentally and there are several models which can predict the microsegregation with different degrees of accuracy [7–15]. The two basic models for analysing solidification process, as defined in Eqs. (1) and (2), are equilibrium and non-equilibrium Lever rules simply called *lever rule* and *Scheil equation*, respectively [16].

$$C_S^{\text{Lever}} = \frac{C_0 k_0}{1 - f_S(1 - k_0)} \tag{1}$$

$$C_S^{\text{Scheil}} = c_0 k_0 (1 - f_S)^{(k_0 - 1)} \tag{2}$$

where C_0, k_0 and f_S are nominal composition of the alloy, partition coefficient, and solid fraction, respectively. These models are still widely used in literature to compare with theoretical and experimental results. By using the electron probe microanalysis (EPMA) inaccuracy of these models has been understood and some

* Corresponding author.Tel./fax: +98 511 8763305.
E-mail addresses: mhgharavol@gmail.com (M.H. Avazkonandeh-Gharavol), haddadm@um.ac.ir (M. Haddad-Sabzevar), hassef@kth.se (H. Fredriksson).

http://dx.doi.org/10.1016/j.jallcom.2014.05.026
0925-8388/

corrections were carried out on these models to consider back diffusion [17], coarsening [18], and undercooling [9].

Solidification behavior of Al alloys has been deeply studied, but the focus is on the Al–Cu [2–4,6,8,13–15,18–22] and Al–Si [20–22] alloys. Solidification of Al–Mg alloys was less studied [3,23] because they need special care for melting and solidification as the Mg is very sensitive to oxidation [1]. Kang and Liu [23], experimentally studied the effects of cooling rate and Mg content on the microstructure and distribution of alloying elements (microsegregation) in the primary phase of Al–Mg alloys in a wide range of compositions and cooling rates. Chen and Huang [3] used thermal analysis for binary Al–Mg alloys with the focus on the calculation of solidification curve, but distribution of alloying elements in the primary phase (concentration profile) was not considered in their work.

The aim of the present research is experimental and numerical analysis of the solidification in binary Al–Mg alloys containing Mg less than the solubility limit at eutectic temperature. Thermal analysis was carried out by a series of the DTA and quenching experiment and numerical modeling. Solidification is analyzed by investigating the solidification path and concentration profile experimentally and theoretically. Microsegregation was studied by SEM/EDX analysis of samples and numerical modeling of the concentration profile in the primary phase. Origin of discrepancies between experimental and numerical results was discussed with respect to diffusion process.

2. Materials and methods

High purity binary Al–Mg alloys were prepared as model alloys. The chemical composition of the alloys was analyzed by optical emission spectrometry (OES). It was determined that the alloys contain 6.7 and 10.2 wt.% Mg and about 0.06 wt.% Fe and 0.05 wt.% Si were also detected which are negligible.

2.1. Thermal analysis

For thermal analysis a DTA furnace with capability of quenching samples during solidification was used. For this purpose, about 1 g of the alloys was melted for each sample, held at 700 °C for 10 min, cooled at rates of 0.5 and 5 K min^{-1}, and quenched from predetermined temperatures during cooling. In each set of experiments one sample was quenched after its complete solidification. High purity argon gas (99.999%), was used during the DTA tests to reduce the risk of oxidation. Samples coding and experimental parameters values are listed in Table 1. Because of the quenching of the samples, furnace was used as reference and its temperature was recorded by a thermocouple similar to the sample thermocouple.

2.2. Microstructure analysis

The microstructure of the samples which are quenched during solidification can be divided into two parts. First part contains coarse primary α-Al dendrites which has been formed before quenching. The second part consists of very fine primary dendrites and eutectic phases which have been formed during quenching. The first part will be called 'primary phase' and the second part 'quenched melt' hereafter.

The samples were prepared for microstructural and compositional analyses by conventional methods. Fractions of the phases were determined by manual swift point counting method based on the ASTM E562-11 standard after etching in 0.5% HF solution. In most of the quenched samples, dendrite arms can be distinguished and their spacing (SDAS) can be easily measured from the optical micrographs. For those samples which the dendrite arms could not be distinguished, because of coalescence of the dendrite arms, samples were etched with Weck's reagent [24].

2.3. SEM analysis

In some of the samples, concentration profiles in the primary phase were determined by SEM/EDX technique. The EDX detector was first calibrated by standard sample containing 4.5 wt.% Mg. In order to have a statistically significant concentration profile in the solid, around 100 points were analyzed by SEM/EDX point analysis technique. These data were processed to obtain concentration profiles in the solid based on the method proposed by Gungor [25].

Table 1
Samples coding and experimental parameters used to prepare them.

Sample code	Mg content (wt.%)	Cooling rate (K min^{-1})	Quenching temperature (°C)
7MgS1		0.5	605
7MgS2			580
7MgS3			540
7MgSF			435
7MgM1	6.7	5	605
7MgM2			580
7MgM3			540
7MgMF			435
10MgS1		0.5	580
10MgS2			540
10MgS3			500
10MgSF			435
10MgM1	10.2	5	580
10MgM2			540
10MgM3			500
10MgMF			435

2.4. Numerical modeling of microsegregation

A numerical model which takes into account the back diffusion in the solid and diffusion in the liquid was used to model the microsegregation during solidification. As the low cooling rates were used, effects of coarsening and eutectic undercooling were ignored [9,26]. To calculate the concentration profiles in the solid and liquid, the Fick's second law, Eq. (3) for solid and Eq. (4) for liquid, was solved separately in the solid and liquid.

$$\frac{\partial C_S}{\partial t} = \left(D_S \frac{\partial^2 C_S}{\partial x^2}\right)_0^{\xi} \tag{3}$$

$$\frac{\partial C_L}{\partial t} = \left(D_L \frac{\partial^2 C_L}{\partial x^2}\right)_{\xi}^{d} \tag{4}$$

where C_S, C_L, D_S, D_L, ξ, and d are concentrations in the solid and liquid, diffusion coefficients in the solid and liquid, position of interface, and length of volume element (which is half of the SDAS), respectively. The mass balance is:

$$\int_0^{\xi} C_S dx_S + \int_{\xi}^{d} C_L dx_L = d \times C_0 \tag{5}$$

Additional mass balance is also needed at the interface according to Eq. (6) [27].

$$\left(D_S \frac{\partial C_S}{\partial x}\right) - \left(D_L \frac{\partial C_L}{\partial x}\right) = (C_L - C_S)\frac{d\xi}{dt} \tag{6}$$

To calculate concentration profiles in the solid and liquid, Eqs. (3)–(6) should be solved. For this purpose a volume element, as shown in Fig. 1, was considered and divided into N nodes: r nodes in solid and $N - r + 1$ in the liquid. Node number r is common between solid and liquid nodes. The solid/liquid interface was considered at node number r. The main assumptions were made to solve the equations are:

1. Mass transfer is controlled by diffusion alone (convection in the liquid is neglected).
2. The dendrites were considered to have a plate-like morphology.
3. The solid/liquid interface is considered to be at local equilibrium so the composition of solid and liquid at the interface can be extracted from the phase diagram.
4. The whole volume element is at uniform temperature (as the heat transfer is several times faster than the mass transfer, so temperature gradient in the volume element is neglected) [27].

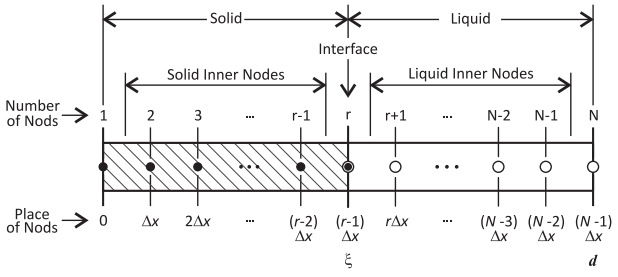

Fig. 1. Schematic of the volume element used for the numerical modeling.

5. There is no mass transfer between the volume element and its surroundings. The flux of alloying element at $x = 0$ and $x = d$ is zero and the Eq. (7) should be fulfilled.

$$\left(\frac{\partial C_S}{\partial x}\right)_{x=0} = \left(\frac{\partial C_L}{\partial x}\right)_{x=d} = 0 \tag{7}$$

For this purpose the compositions of the nodes number 1 and N were considered to be equal to the compositions of the nodes number 2 and $N-1$, respectively.

Boundary Conditions: According to assumptions number 3 and 5 the required boundary conditions for each phase are based on Eqs. (8)–(11).

$$(C_S)_1^t = (C_S)_2^t \tag{8}$$

$$(C_S)_r^t = (C_S)_{Eq}^t \tag{9}$$

$$(C_L)_r^t = (C_L)_{Eq}^t \tag{10}$$

$$(C_L)_N^t = (C_L)_{N-1}^t \tag{11}$$

So the Eqs. (3)–(6) were solved for nodes number 2 to $r-1$ in solid and $r+1$ to $N-1$ in the liquid.

Implementation of the model: The concentration profiles in the solid and liquid were calculated by rewriting the finite deference forms of the Eqs.)(3)–(6) and solving them by a mesh contracting/expanding explicit numerical scheme proposed by Tanzilli and Heckel [28]. Based on the preliminary calculations, the accuracy is acceptable for 50 nodes in the solid and 10 nodes in the liquid. The initial conditions were sat for liquidus temperature and then main calculations start and continue until the composition of melt reaches to the eutectic composition or $\delta = d$. Time step was calculated according to the stability criterion [29]. In each time step the position of the interface is calculated by solving Eq. (6) and concentration profiles in the solid and liquid are calculated by solving Eqs. (3) and (4), respectively. Mass conservation law is checked according to Eq. (5) and if it is fulfilled, previous values of the parameters (position of the S/L interface and concentration profile in the solid and liquid) are replaced by the new calculated values. However, if the mass is not conserved, the exact position of the S/L interface is determined by solving Eq. (5) and considering δ as unknown parameter, and the calculations of this time step will be repeated again. The next temperatures are calculated according to the cooling scheme and the main calculations for the new time steps are performed as explained above. The calculations continue until the melt composition reaches to the eutectic composition or $\delta = d$. Parameters which were used in the model are reported in Table 2 [30–32].

3. Results and discussion

3.1. Thermal analysis

Some examples of cooling curves for 10 MgM series are shown in Fig. 2. The cooling curves are smooth and reproducible. Quenching temperatures are indicated by arrows. The DTA curves of the samples quenched after complete solidification can be seen in Fig. 3. The data which are extracted from DTA analysis are presented in Table 3. In the DTA curve of 7MgSF, two peaks can be seen which are started at 619.5 and 484 °C and they are due to the start and the end of the solidification of α-Al phase, respectively. Several peaks can be seen at 440–460 °C which look like

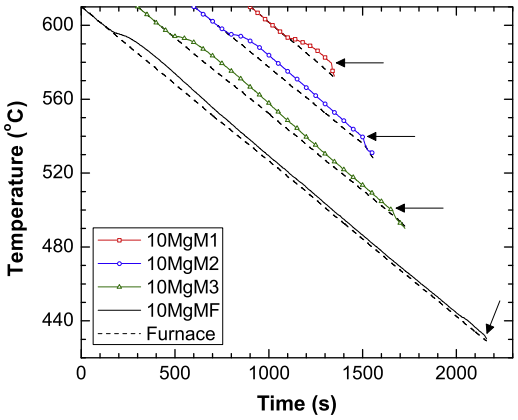

Fig. 2. Cooling curves of 10MgM series. Quenching is indicated by arrows.

thermal fluctuations. In 7MgMF curve, just one peak can be seen which is started at 614.5 °C and corresponds to the start of the solidification of α-Al phase. For 10Mg series at both cooling rates, two peaks can be seen in DTA curves. In 10MgSF curve, the first peak is started at 598.5 °C for starting of the solidification of the α-Al phase and the second one is started at 446 °C for the eutectic reaction. By increasing the cooling rate, both peaks are appeared at lower temperatures and in 10MgMF DTA curve, they are started at 595 and 442 °C for starting of the solidification of the α-Al and eutectic reaction, respectively.

The shapes of the DTA curves are somehow different in 0.5 and 5 K min^{-1}. In 0.5 K min^{-1} curves, the peaks for the beginning of the solidification are sharp. It may be related to the difference in the cooling rates [33]. In 7MgSF curve, a very broad peak can be seen after the beginning of the solidification at around 600–570 °C which can also be seen in other samples in this series as is demonstrated in Fig. 4. In this figure, quenching and the broad peak are indicated by black and hallow arrows, respectively. It seems that this peak does not correspond to any transformation in the sample and it should be a feature of this alloy in this cooling rate. This will be discussed in the next section.

3.2. Microstructural analysis

The microstructures of the quenched samples are shown in Figs. 5 and 6. The results of quantitative metallography are presented in Table 4. According to Figs. 5 and 6, in both alloys and at both cooling rates, there are just two microstructural constituents in all quenching temperatures, i.e. primary (α-Al) phase (white phase) and the quenched melt (dark phase). Microstructure of the quenched melt is shown in Fig. 7-(a). This image is an

Table 2
Input parameters in microsegregation model.

Parameter	Units	Value	Reference
Al molar weight	g	26.981	[30]
Mg molar weight		24.305	
Al density	g cm^{-3}	2.7	
Mg density		1.738	
D^S_{Mg}	$(\mu m)^2$ s^{-1}	$6.23 \times 10^6 \exp\left(-\frac{1.15\times10^5}{RT}\right)$	[30]
D^L_{Mg}		$9.9 \times 10^7 \exp\left(-\frac{7.16\times10^4}{RT}\right)$	[30]
Eutectic temperature	°C	450	[32]
Eutectic composition	wt.-%	35.6	
Solidus equation[a]	wt.-%	$w_S = 1.827 \times 10^{-4} \times T^2 - 0.283 \times T + 106.875$	
Liquidus equation[a]	wt.-%	$w_L = -2.394 \times 10^{-5} \times T^2 - 0.144 \times T + 105.535$	

[a] Temperature are in °C.

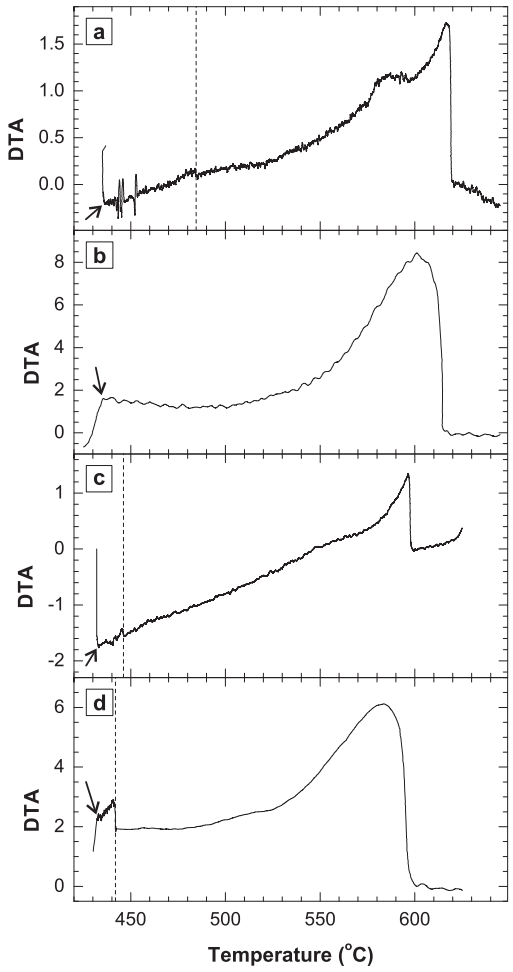

Fig. 3. DTA curves of (a) 7 MgSF (b) 7MgMF, (c) 10 MgSF, and (d) 10 MgMF.

example of 10MgS2 microstructure and the other quenched samples have the same microstructural constituents. According to Fig. 7-(a), quenched melt is consisted of two parts:

1. Primary α-Al phase which formed during quenching (phase #2) and it is extremely finer than the primary α-Al phase which formed before quenching (phase #1).
2. Secondary phase which is a part of the eutectic phases (phase #3).

In Fig. 7-(a), the dashed lines show the approximate boundaries between the primary phases and the quenched melt. The α-Al phase which formed during quenching cannot be distinguished from the eutectic α phase. In Fig. 7-(b), SEM micrograph of the quenched melt inside a crack in 7MgS1 sample is presented which shows the morphology of the dendrites in the quenched part.

Based on the Figs. 5 and 6 and Table 4, by increasing cooling rate or Mg content, the scale of microstructure becomes finer and the

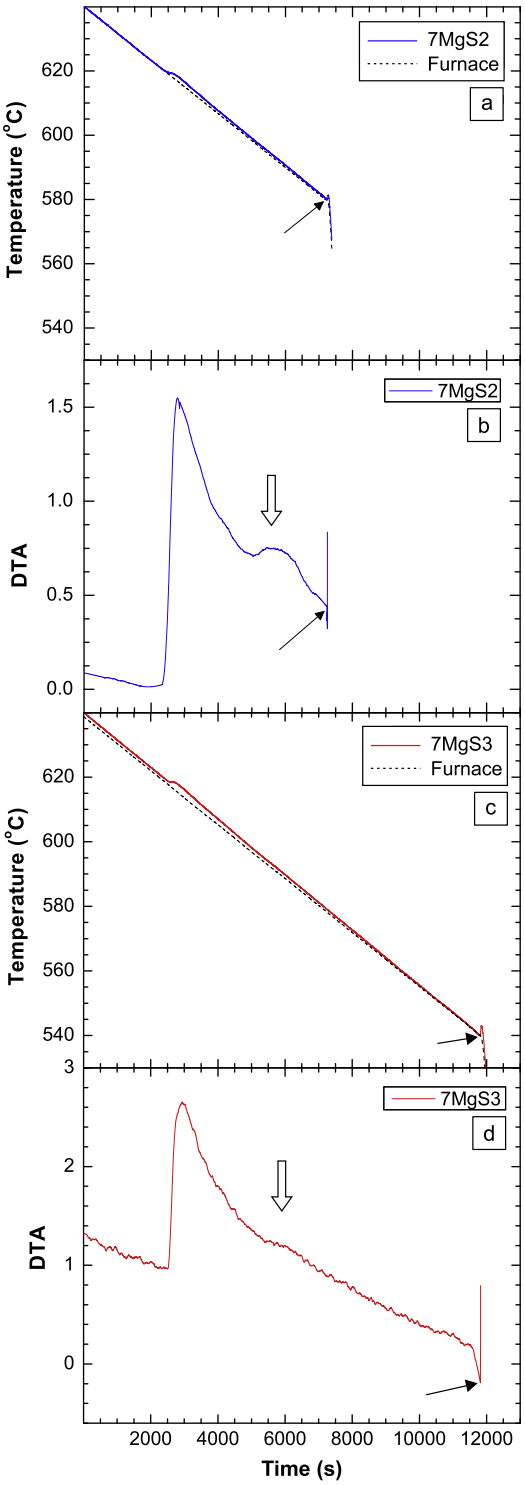

Fig. 4. (a) and (b) cooling and DTA curves of 7 MgS2 and (c) and (d) cooling and DTA curves of 7MgS3 samples, respectively. Quenching and broad peak are indicated by black and hallow arrows.

Table 3
Results of thermal analysis.

Alloy code	Cooling rate (K min^{-1})	Solidification start temperature (°C)	Eutectic start temperature (°C)	Solidification range (°C)	Primary undercooling (°C)	Solidification time (s)
7Mg	0.5	619.5	–	135.5	1.6	16,260
	5	614.5	–	–	5.4	–
10Mg	0.5	598.5	446	152.5	2.3	18,120
	5	595	442	153	5.3	1883

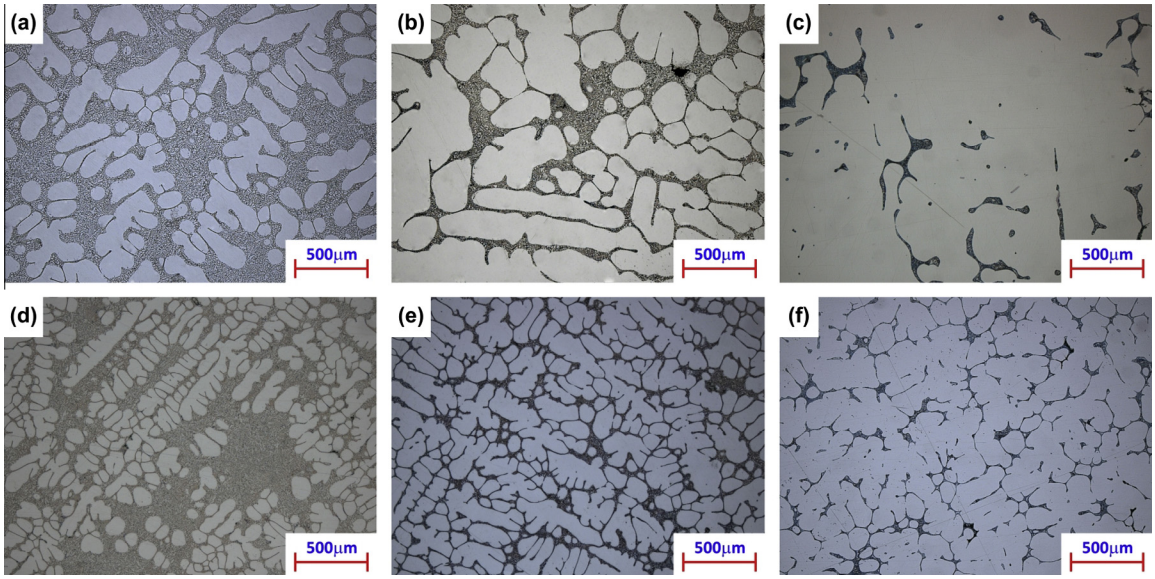

Fig. 5. Microstructure of quenched samples of 7Mg alloy. (a) 7MgS1, (b) 7MgS2, (c) 7MgS3, (d) 7MgM1, (e) 7MgM2, and (f) 7MgM3.

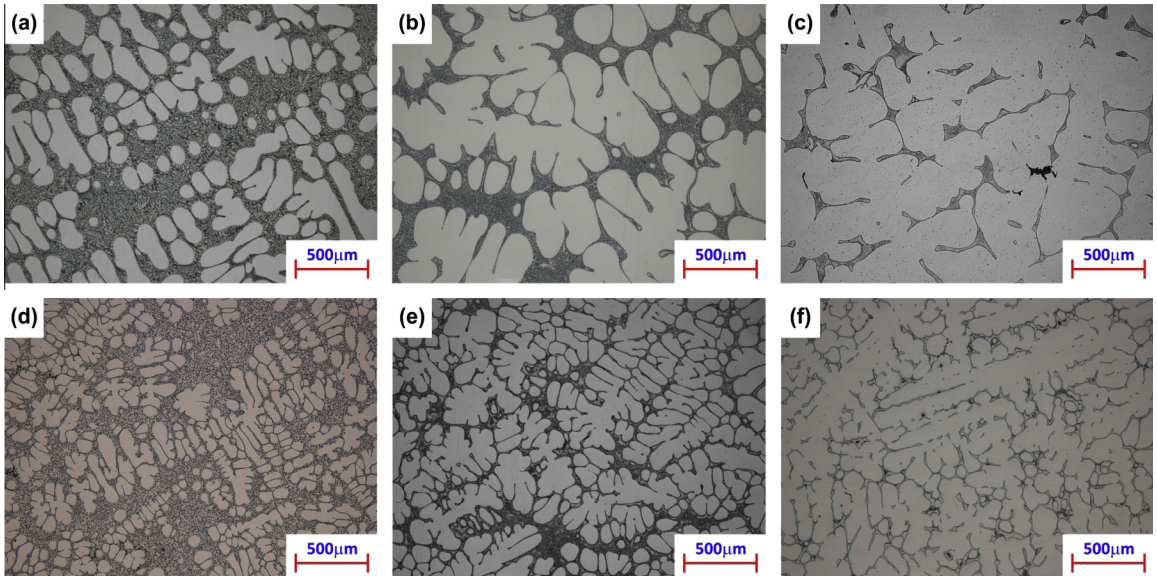

Fig. 6. Microstructure of quenched samples of 10 Mg alloy. (a) 10MgS1, (b) 10MgS2, (c) 10MgS3, (d) 10MgM1, (e) 10MgM2, and (f) 10MgM3.

Table 4
Results of quantitative metallography.

Sample code	f_α[a] (wt.%)	SDAS (μm)
7MgS1	55.8	93.2
7MgS2	76.4	143.2
7MgS3	92.3	170.4
7MgSF	100	240.0
7MgM1	59.8	51.5
7MgM2	75.8	68.6
7MgM3	87.3	95.9
7MgMF	100	101.5
10MgS1	48.6	99.2
10MgS2	73.3	139.8
10MgS3	86.0	170.4
10MgSF	98.5	200.0
10MgM1	47.2	48.8
10MgM2	70.8	65.2
10MgM3	85.6	74.2
10MgMF	97.8	78.7

[a] Fraction of the primary phase.

effect of the Mg content is more severe at higher cooling rates. In 0.5 K min^{-1}, the dendrites are more globular and with increasing the cooling rate to 5 K min^{-1} their size severely decreases but the branching frequency increases.

According to the results of thermal (Fig. 3) and microstructural (Figs. 5 and 6) analyses, the evolution of the microstructure in these alloys can be described as below. As the melt temperature reaches to liquidus temperature, the primary phase nucleates. Fraction of the solid (primary phase) increases continuously until the end of solidification. If the melt composition reaches to the eutectic composition, eutectic transformation will occur (10 Mg alloy at both cooling rates) otherwise it will solidify as a single phase alloy, as in the case of 7 Mg alloy at both cooling rates. Based on these results, the broad peak in the DTA curve of 7MgSF, as mentioned before, should be a feature of this alloy in this cooling rate. The origin of the broad peak is not clear to the authors. Each peak in a DTA curve corresponds to a transformation in the sample. As the samples quenched at temperatures lower than the

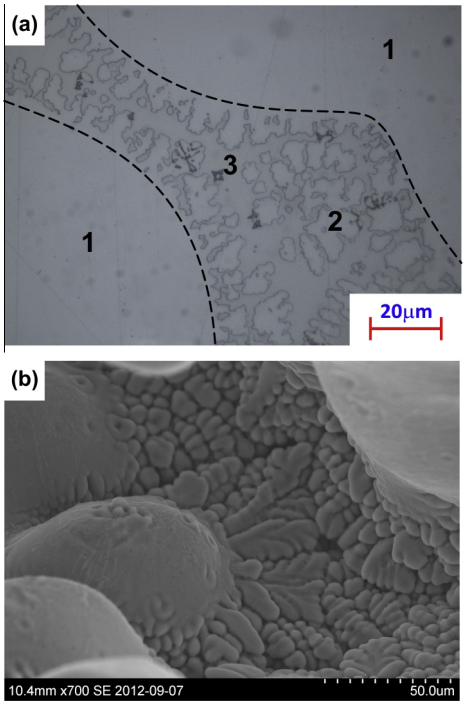

Fig. 7. Structure of the quenched melt. (a) Optical micrograph of 10MgS2 and (b) SEM micrograph of 7 MgS1.

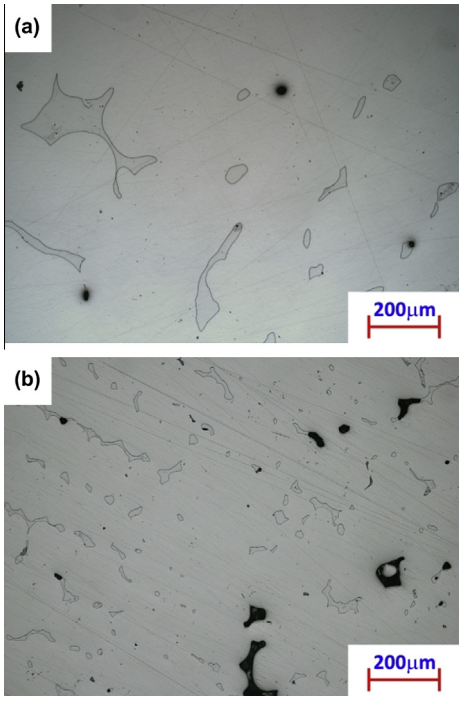

Fig. 8. Microstructure of the samples of 10 Mg alloy which did not quenched during solidification. (a) 10MgSF and (b) 10MgMF.

temperature range of this peak (7MgS2 and 7MgS3) show the same microstructural constituents as 7MgS1, so the broad peak does not correspond to any transformation in the sample. Moreover, it cannot be seen in 7MgM series or in 10 Mg alloy samples.

So 7 Mg series samples solidify as single phase alloy at both cooling rates and there is no eutectic constituent in the microstructure. However, the microstructures of 10 Mg samples, as can be seen in Fig. 8, are consisted of primary α-Al phase and the Mg rich second phase. Some shrinkage pores can also be seen in their microstructures.

In Fig. 9, experimental solid fractions are compared with the solidification curves which are calculated by numerical method and the well-known Lever rule and Scheil equation. The curves for lever rule and Scheil equation are calculated by the solid fraction versus temperature ($f_S - T$) forms of the Eqs. (1) and (2) which are written as Eqs. (12) and (13) [34].

$$f_S^{\text{Lever}} = \frac{1}{1-k_0} - \frac{T_m - T_0}{(1-k_0)(T_m - T)} \tag{12}$$

$$f_S^{\text{Scheil}} = 1 - \left(\frac{T_m - T}{T_m - T_0}\right)^{\frac{-1}{1-k_0}} \tag{13}$$

where f_S^{Lever}, f_S^{Scheil}, T_m, T_0, and T are solid fractions according to lever rule and Scheil equation, melting point of the solvent (aluminum), liquidus temperature of the alloy, and temperature, respectively. In order to use Eqs. (12) and (13), it was assumed that the partition coefficient is constant and equal to 0.47. In most cases these equations cannot estimate the solidification path very accurately. It is because of nonrealistic assumptions of infinite and zero diffusion coefficients in the solid for Lever rule and Scheil equation, respectively. They just show the upper and lower boundaries for solidification curves. Based on the lever rule both alloys should have single phase solidifications. However, according to Scheil equation both alloys have a eutectic transformation at the end of their solidifications and eutectic content increases with increasing the Mg content. Results of the numerical modeling, which considers back diffusion in the solid, show much better consistency with experimental results (especially at medium temperatures) but there are still some deviations at very high or low temperatures. The results of these calculations also prove the single phase solidification of 7 MgSF series. According to these calculations, both 10 MgS and 10MgM series undergo a eutectic transformation at the end of their solidifications but the predicted eutectic contents by the model are more than the experimental values. Chen and Huang [3] also modeled the solidification curves in their work but they did not achieve good correlation between the experimental and modeling results compared to the current results. They employed a heat transfer model to calculate solidification curve, but according to the current results, it seems that the present model which is based on mass transfer gives rise to better consistency between the experimental and modeling results.

The results of SDAS measurement are presented in Table 4. It can be seen that by increasing the cooling rate and Mg content, SDAS decreases. Eq. (14) is commonly used to estimate SDAS value [35].

$$\lambda^3 - \lambda_0^3 = k' \times t \tag{14}$$

where λ, λ_0, k', and t are SDAS, SDAS at the beginning of the solidification, coarsening constant, and time, respectively. λ_0 is an important parameter at the early stages of solidification where its magnitude is comparable to λ value and its value is considered twice the dendrite tip radius by Kraft et al. [9]. In this study it is neglected so the Eq. (14) can be rearranged as Eq. (15).

$$\lambda = k \times t^{0.33} \tag{15}$$

If the effect of alloy composition is also considered, the Eq. (16) can be used to calculate SDAS value [7].

$$\lambda = k \times t^{0.33} \times C_0^{-m} \tag{16}$$

where C_0 is nominal concentration of Mg in the alloy and k and m are adjustable parameters which should be determined according to experimental data. In the present study k and m are calculated by least square method to be 16.9 and 0.32, respectively.

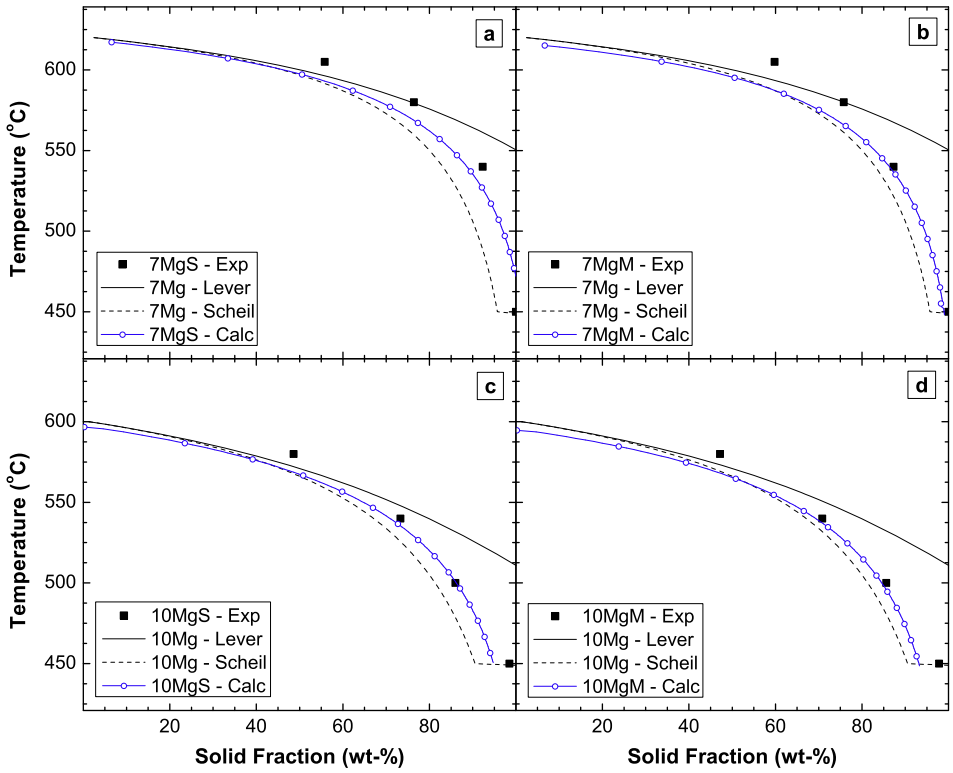

Fig. 9. Experimental solid fraction in comparison with the results of calculation based on the Lever rule, Scheil equation, and the numerical modeling for (a) 7 MgS, (b) 7MgM, (c) 10 MgS, and (d) 10MgM.

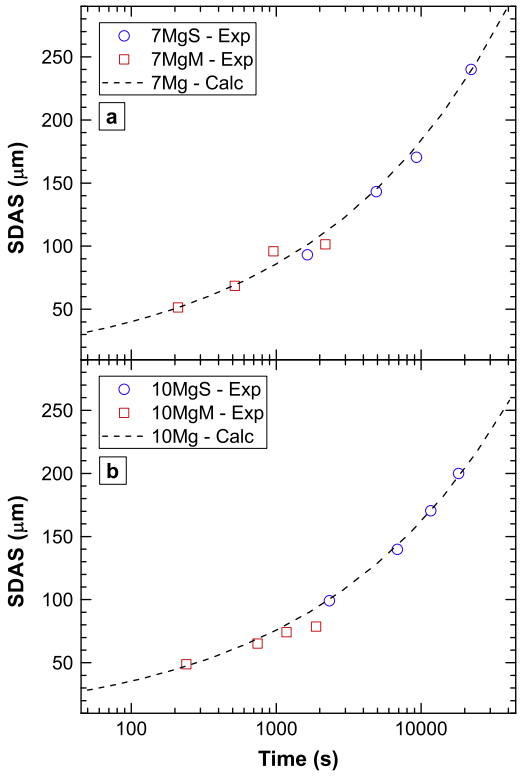

Fig. 10. Experimental results of SDAS in comparison with the calculated results for (a) 7Mg and (b) 10Mg alloys.

The experimental and calculated SDAS values are shown in Fig. 10 and it can be seen that the experimental results can be accurately estimated by Eq. (16).

3.3. SEM/EDX analysis

Experimental concentration profiles are shown in Fig. 11. In this figure, three other curves based on the Lever rule and Scheil equation are also plotted for comparison. The curves which named "Scheil equation" and "Lever rule – interface" were plotted by using of Eqs. (1) and (2) and assuming k_0 is constant and equal to 0.47. Former curve shows the distribution of Mg atoms across the secondary dendrite arms after the end of solidification according to Scheil equation and the latter one shows Mg concentration in the solid at solid/liquid interface during solidification based on the Lever rule. The "Lever rule" line shows the distribution of the Mg atoms across SDAS, after the end of solidification according to Lever rule, which there is no concentration gradient accordingly. Based on Fig. 11, all experimental profiles deviate from Scheil equation curve which shows considerable diffusion in the solid for these alloys. In both 7Mg and 10Mg alloys, by increasing the cooling rate from 0.5 to 5 K min^{-1}, the beginning of the profiles reduce to lower and their end increase to higher concentrations. It is due to the reduction of back diffusion with increasing cooling rate which causes less Mg in the solid and more Mg in the melt. So at the beginning of solidification (or at low solid fractions) in 5 K min^{-1}, the Mg concentration in the solid is less than that of the 0.5 K min^{-1}. However, as the solidification proceeds, in 5 K min^{-1}, the pile up of the Mg atoms in the melt at solid/liquid interface is more than that of the 0.5 K min^{-1} so the solid which formed at last stages of solidification in 5 K min^{-1} has higher Mg content than the 0.5 K min^{-1}. In 5 K min^{-1}, there is not enough time for Mg atoms near solid/liquid interface to diffuse back and even out the concentration gradient of Mg in the solid at last stages of solidification. With increasing the Mg content, profiles increases to higher concentrations.

The calculated concentration profiles are shown in Fig. 12. Based on this figure, by considering back diffusion in the numerical

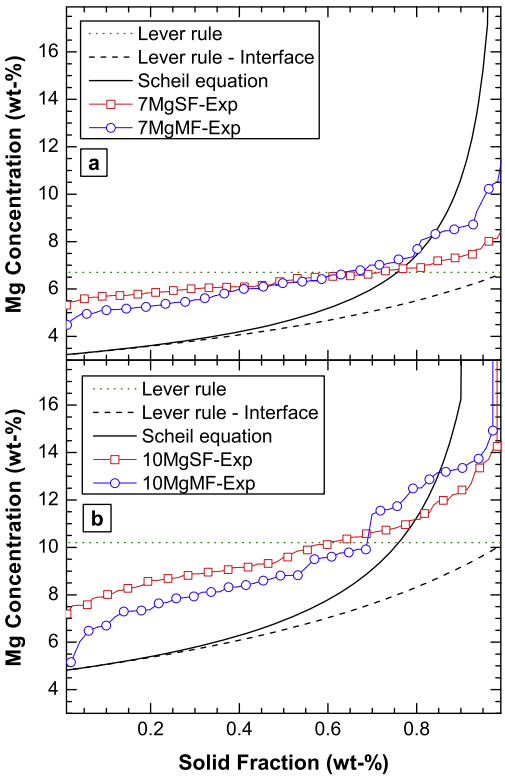

Fig. 11. Experimental concentration profiles of (a) 7Mg and (b) 10Mg alloy.

modeling, the experimental results can be modeled with more accuracy than the Scheil equation but still there is too much deviations. Modeling results show more segregation than the experimental results. In 0.5 K min^{-1} effect of back diffusion is more pronounced and the calculated profiles move to higher concentrations at low solid fractions compared to Scheil equation. But by increasing the cooling rate to 5 K min^{-1} effect of back diffusion on the profile reduces and numerical results correlate well with the Scheil equation at low solid fractions.

Different mechanisms which may affect microsegregation in the alloys (the distribution of alloying elements in the primary phase and fraction of the non-equilibrium second phase) are mainly back diffusion [17], coarsening [18], and eutectic undercooling [9,26]. Back diffusion is important at low to medium and coarsening and eutectic undercooling in medium to high cooling rates [9,26,36]. So it seems reasonable to just consider back diffusion and ignoring the other parameters in the present work. But several researchers in recent years have noticed that the inconsistency between experimental and modeling results may come from the data used in the modeling including phase diagram [13,37,38] and diffusion coefficient [5,13,39]. Chang and his colleagues [37,38] modified the solidus line of the Al-rich part of the binary Al–Cu phase diagram and used this new phase diagram to model the microsegregation in Al–Cu and Al–Cu–Mg alloys. They showed that the calculations based on the new phase diagram show better correlation with the experimental results. Hunt and his co-workers [13] also modified binary Al–Cu phase diagram (the solvus line) and measured the diffusion coefficient and used their new data to model the microsegregation in the binary Al–Cu alloys. They also found better consistency between the experiments and calculations by their new data [13]. Fredriksson and his colleagues [19–21,40–43] proposed a new solidification model which considers the effect of non-equilibrium defects (especially excess vacancies) formed during solidification on the solidification behavior of aluminum and copper alloys [19–21,40–42]. They showed that different features like undercooling [41], heat of fusion [42], phase diagram (and hence partition coefficient) [19–21,40,42], and

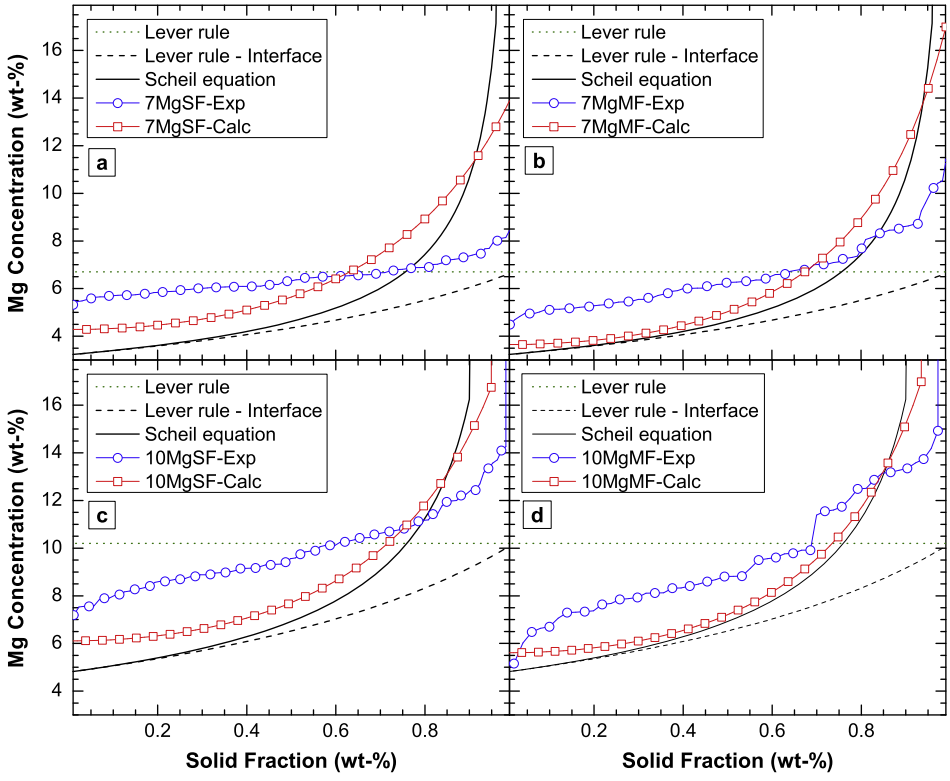

Fig. 12. Calculated profiles in comparison with the experimental profiles for (a) 7MgSF, (b) 7MgMF, (c) 10MgSF, and (d) 10MgMF.

diffusion coefficient [39] can be changed by the existence of these defects during solidification. So it seems reasonable to discuss the effect of these parameters on the solidification of Al–Mg alloys studied in the present work. The main focus is on the diffusion coefficient and effect of the excess vacancies on the phase diagram is ignored. The aim is not to determine a new value for diffusion coefficient and this is just a discussion to elucidate the microsegregation mechanism.

According to Fig. 11, the concentration profile of 7MgSF is very plateau and it seems that the Mg atoms are uniformly distributed in the solid. This profile looks like an ideal distribution of the atoms when the diffusion coefficient is considered to be infinite in the solid (as the situation for the Lever rule). It implies that the diffusion coefficient may be higher than the value used in the present work which is extracted from [30]. So if the diffusion coefficient is increased (doubled here) and the profiles are calculated by this doubled diffusion coefficient, as can be seen for 5 K min^{-1} in Fig. 13-(a), much better consistency between experimental and calculated profiles can be achieved. In Fig. 13-(b) the results of calculation of the solidification curve by doubling the diffusion coefficient is shown and it can be seen that better correlation is also achieved in this case especially at the end of solidification. Increase in the diffusion coefficient is related to the increase in the defects content in the solid during solidification. For simplicity these defects can be considered as vacancies. The vacancy content at the solid/liquid interface may be much higher than the equilibrium values [43]. These excess vacancies can be sank to the equilibrium value behind the interface depending on the situations, such as solidification rate but during the solidification they can change some parameters such as partition coefficient [21,42] and diffusion coefficient [5,39]. The vacancy content cannot be measured directly during solidification but the current results indirectly show that the diffusion coefficient can be higher than the equilibrium values as it suggested before [5,39].

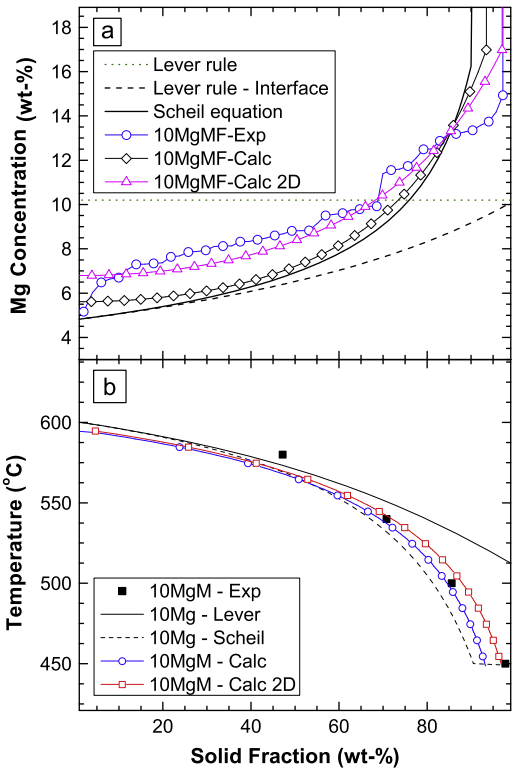

Fig. 13. Comparison between the experimental results and calculated results by using doubled diffusion coefficient for (a) concentration profile of 10MgMF and (b) solidification curves of 10MgM series.

4. Conclusion

Solidification of binary Al–Mg alloys containing 6.7 and 10.2 wt.% Mg was studied by thermal analysis, metallography, and SEM/EDX analysis in 0.5 and 5 K min^{-1} cooling rates. Following conclusions can be drawn from this study.

1. According to the experimental results, the alloy containing 6.7 wt.% Mg solidifies as a single phase alloy and the solidification of the alloy containing 10.2 wt.% Mg ends with a eutectic reaction (multiphase alloy) at both cooling rates. Calculated solidification paths confirm these results and agree well with them quantitatively at medium temperatures.
2. By increasing the cooling rate (from 0.5 to 5 K min^{-1}) and Mg content (from 6.7 to 10.2 wt.% Mg) SDAS decreases. The coarsening constant and exponent are calculated to be 16.9 and 0.32, respectively.
3. By increasing the cooling rate (from 0.5 to 5 K min^{-1}) the beginning of the concentration profiles reduces to lower concentrations and the end of the profile increases to higher concentrations due to reduction of back diffusion. By increasing the Mg content, the concentration profiles increases to higher concentrations.
4. Results of numerical simulation which considers back diffusion in the solid show that by using the tabulated diffusion data the experimental results cannot be estimated with enough precision. It seems that the diffusion coefficient should be increased somehow to have good correlation between experimental and modeling results.

Acknowledgment

The technical support of the Royal Institute of Technology for performing the experiments is appreciated. M.H. Avazkonandeh-Gharavol appreciates the financial support by Ministry of Sciences, Research and Technology of Islamic Republic of Iran during his visit to the Royal Institute of Technology. Haji Muhhamad Muhmond and Saud Salim are also gratefully acknowledged for help to set up the experiments.

References

[1] I.J. Polmear, Light Alloys: From Traditional Alloys to Nanocrystals, fourth ed., Butterworth-Heinemann publications, MA, 2006.
[2] O. Fornaro, H.A. Palacio, Study of dilute Al–Cu solidification by cooling curve analysis, J. Mater. Sci. 44 (2009) 4342–4347.
[3] S.-W. Chen, C.-C. Huang, Solidification curves of Al–Cu, Al–Mg and Al–Cu–Mg alloys, Acta Mater. 44 (1996) 1955–1965.
[4] H.B. Dong, M.R.M. Shin, E.C. Kurum, H. Cama, J.D. Hunt, Determination of liquid fraction during solidification of aluminium alloys using a single-pan scanning calorimeter, Fluid. Phase. Equilibria 212 (2003) 199–208.
[5] T. Antonsson, H. Fredriksson, The effect of cooling rate on the solidification of INCONEL 718, Metall. Mater. Trans. B 36 (2005) 85–96.
[6] H.B. Dong, M.R.M. Shin, E.C. Kurum, H. Cama, J.D. Hunt, A study of microsegregation in Al–Cu using a novel single-pan scanning calorimeter, Metall. Mater. Trans. A 34 (2003) 441–447.
[7] A. Roosz, E. Halder, H.E. Exner, Numerical calculation of microsegregation in coarsened dendritic microstructures, Mater. Sci. Technol. 2 (1986) 1149–1155.
[8] V.R. Voller, S. Sundarraj, Modeling of microsegregation, Mater. Sci. Technol. 9 (1993) 474–481.
[9] T. Kraft, M. Rettenmayr, H.E. Exner, An extended numerical procedure for predicting microstructure and microsegregation of multicomponent alloys, Modell. Simul. Mater. Sci. Eng. 4 (1996) 161–177.
[10] A. Turkeli, Approximate analytical models for microsegregation considering the effect of dendrite arm coarsening, Mater. Sci. Forum 508 (2006) 449–454.
[11] Q. Du, A. Jacot, A two-dimensional microsegregation model for the description of microstructure formation during solidification in multicomponent alloys: formulation and behavior of the model, Acta Mater. 53 (2005) 3479–3493.
[12] J. Tang, X. Xue, Numerical simulation of multi-grain structure and prediction of microsegregation in binary Ni–Cu alloy under isothermal conditions, Mater. Sci. Eng. A 499 (2009) 64–68.

[13] E.C. Kurum, H.B. Dong, J.D. Hunt, Microsegregation in Al–Cu alloys, Metall. Mater. Trans. A 36 (2005) 31033110.
[14] D. Eskin, Q. Du, D. Ruvalcaba, L. Katgerman, Experimental study of structure formation in binary Al–Cu alloys at different cooling rates, Mater. Sci. Eng. A405 (2005) 1–10.
[15] Q. Du, D.G. Eskin, A. Jacot, L. Katgerman, Two-dimensional modeling and experimental study on microsegregation during solidification of an Al–Cu binary alloy, Acta Mater. 55 (2007) 1523–1532.
[16] M.E. Glicksman, R.N. Hills, Non-equilibrium segregation during alloy solidification, Philos. Mag. A 81 (2001) 153159.
[17] M.C. Flemings, Solidification Processing, McGrowHill, NY, 1974.
[18] A. Mortensen, On the influence of coarsening on microsegregation, Metall. Trans. A 20 (1989) 247253.
[19] S. Berg, J. Dahlström, H. Fredriksson, The influence of lattice defects on the solidification process of Al–Cu alloys, ISIJ Int 35 (1995) 876885.
[20] J. Fjellstedt, H. Fredriksson, On the crystallization process of hypoeutectic Al–6% Cu, unmodified and Sr, modified Al–2% Si solidified alloys, Adv. Eng. Mater. 5 (2003) 2432.
[21] J. Fjellstedt, H. Fredriksson, An Experimental and Theoretical Study of the Microsegregation in Al–6% Cu and Al–2% Si Alloys, in: Proceeding of the international conference on solidification science and processing: outlook for the 21st century, Bangalore, India, February 2001, p. 1821.
[22] J.A. Sarreal, G.J. Abbaschian, The effect of solidification rate on microsegregation, Metall. Trans. A 17 (1986) 20632073.
[23] Y.L. Liu, S.B. Kang, Solidification and segregation of Al–Mg alloys and influence of alloy composition and cooling rate, Mater. Sci. Technol. 13 (1997) 331–336.
[24] ASM committee on aluminium alloys, Aluminium Alloys, in: G.F. Vander Voort (Ed.), ASM handbook, ninth ed., vol. 9, Metallography and Microstructures, ASM International, OH, 1992.
[25] M.N. Gungor, A statistically significant experimental technique for investigating microsegregation in cast alloys, Metall. Trans. A 20 (1989) 25292533.
[26] T. Kraft, A. Roosz, M. Rettenmayr, Undercooling effects in microsegregation modelling, Scripta Mater. 35 (1996) 7782.
[27] S. Sundarraj, V.R. Voller, The binary alloy problem in an expanding domain: the microsegregation problem, Int. J. Heat Mass Trans. 36 (1993) 713723.
[28] R.A. Tanzilli, R.W. Heckel, Numerical solutions to the finite, diffusion-controlled, two-phase, moving-interface problem (with planar, cylindrical, and spherical interfaces), Trans. AIME 242 (1968) 2312–2321.
[29] M. Rappaz, M. Bellet, M. Deville, Numerical Modeling in Materials Science and Engineering, Springer-Verlag, Berlin, 2003.
[30] W.F. Gale, T.C. Totemeier, Smithells Metals Reference Book, eighth ed., Elsevier Butterworth-Heinemann Publications, USA, 2004.
[31] Y. Du, Y.A. Chang, B. Huang, W. Gong, Z. Jin, H. Xu, Z. Yuan, Y. Liu, Y. He, F.-Y. Xie, Diffusion coefficients of some solutes in fcc and liquid Al: critical evaluation and correlation, Mater. Sci. Eng. A 363 (2003) 140–151.
[32] ASM handbook, vol. 3, Alloy phase diagrams, tenth ed., H. Baker, H. Okamoto, (Eds.), ASM international, Ohio, 1992.
[33] M.H. Braga, L.F. Malheiros, J.M.V. Machado, O.M. Freitas, Relationship between the DTA peak and the phase diagram: symbiosis between a thermodynamic database and a DTA curve, J. Mater. Process. Technol. 92–93 (1999) 31–34.
[34] H. Fredriksson, U. Akerlind, Materials Processing During Casting, John Wiley & Sons Ltd. publication, UK, 2006.
[35] H. Fredriksson, U. Akerlind, Solidification and Crystallization Processing in Metals and Alloys, John Wiley & Sons Ltd. publication, UK, 2012.
[36] T. Kraft, Y.A. Chang, Discussion of "Effect of Dendrite Arm Coarsening on Microsegregation", Metall. Mater. Trans. A 29 (1998) 24472449.
[37] X. Yan, F. Xie, M. Chu, Y.A. Chang, Microsegregation in Al–4.5Cu wt.% alloy: experimental investigation and numerical modeling, Mater. Sci. Eng. A302 (2001) 268–274.
[38] H. Liang, T. Kraft, Y.A. Chang, Importance of reliable phase equilibria in studying microsegregation in alloys: Al–Cu–Mg, Mater. Sci. Eng. A 292 (2000) 96–103.
[39] A. Formenti, A. Eliasson, H. Fredriksson, On the Dendritic Growth and Microsegregation in Ni-Base Superalloys In718, In625 and In939, High Temp. Mater. Process. 24 (2005) 221–238.
[40] M. Haddad-Sabzevar, PhD Thesis, Royal Institute of Technology (KTH), Stockholm, 1994.
[41] J. Mahmoudi, H. Fredriksson, Modelling of solidification for copper-base alloys during rapid solidification processing, Mater. Sci. Eng. A (2227) (1997) 226–228.
[42] J. Mahmoudi, H. Fredriksson, Thermal analysis of copper–tin alloys during rapid solidification, J. Mater. Sci. 35 (2000) 4977–4987.
[43] H. Fredriksson, N. Jacobson, The effect of interface kinetics on crystallization processes of alloys at high cooling rate, Key Eng. Mater. (5970) (1993) 871–883.